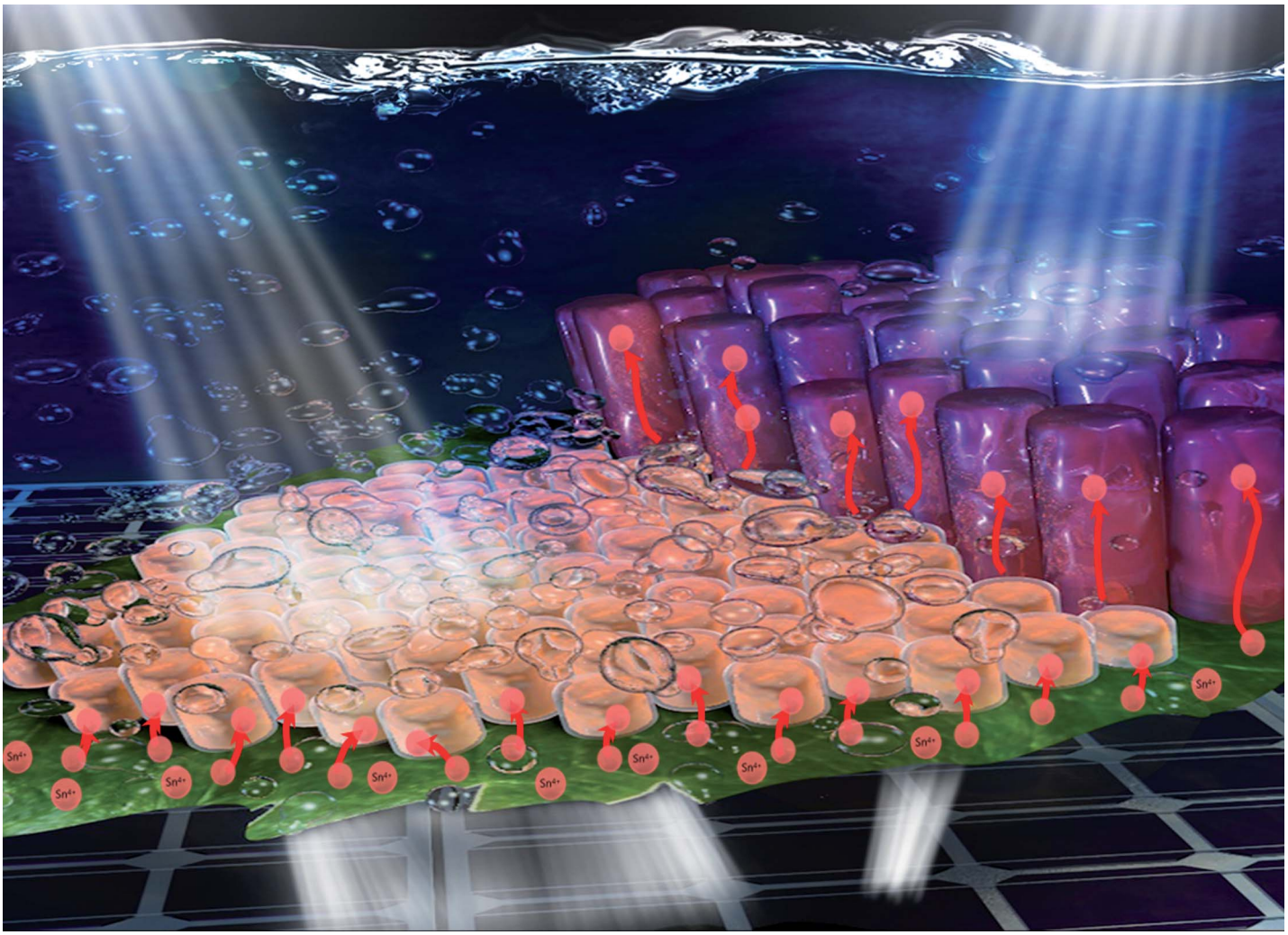

Highlighting a study on a key factor for heteroatom doping on hematite photoanodes from the laboratory of Prof. Ji-Hyun Jang in the Department of Energy Engineering at Ulsan National Institute of Science and Technology (UNIST) in Republic of Korea.

Recent progress and perspectives on heteroatom doping of hematite photoanodes for photoelectrochemical water splitting

This report provides a comprehensive overview of the heteroatom doping effect on hematite, with a focus on diffusion primarily from the fluorine-doped tin oxide glass substrate.

As featured in:

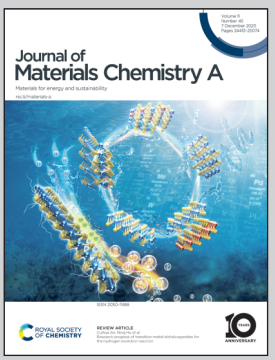

See Ji-Hyun Jang *et al.*, *J. Mater. Chem. A*, 2023, **11**, 24551.

ROYAL SOCIETY OF CHEMISTRY

rsc.li/materials-a

Registered charity number: 207890

Journal of Materials Chemistry A

ROYAL SOCIETY OF CHEMISTRY

PERSPECTIVE

View Article Online
View Journal | View Issue

Cite this: J. Mater. Chem. A, 2023, 11, 24551

Recent progress and perspectives on heteroatom doping of hematite photoanodes for photoelectrochemical water splitting

Juhyung Park, Jihun Kang, Sourav Chaule and Ji-Hyun Jang *

Received 30th July 2023
Accepted 8th October 2023

DOI: 10.1039/d3ta04520j

rsc.li/materials-a

Over the past few decades, extensive research on photoelectrochemical (PEC) water splitting has been conducted as a promising solution to meet the increasing demand for cleaner and renewable energy in a sustainable manner. Among the various photocatalysts, hematite (α-Fe_2O_3) has gained significant attention due to its advantageous characteristics, such as a high theoretical solar-to-hydrogen conversion efficiency value, a suitable band gap energy for visible light absorption, chemical stability, and low cost. However, the high PEC potential of α-Fe_2O_3 is hindered by several limitations, including band gap mismatch, short hole diffusion length, and low electrical conductivity. Several modifications are necessary to enhance the viability of α-Fe_2O_3 as an efficient photocatalyst for PEC water splitting. This review article primarily focuses on strategies aimed at improving PEC water oxidation performance, especially by addressing its poor transport behavior through heteroatom doping. In particular, we explore the co-doping approach involving unintentional Sn dopants, which are diffused from the fluorine-doped tin oxide substrate during high-temperature annealing.

1. Introduction

With the increasing global demand for energy, solar energy has received significant attention as a clean and infinite energy source. Since the development of the photoelectrochemical (PEC) water splitting technology by Fujishima and Honda in 1972, PEC water splitting has emerged as one of the most promising strategies for converting solar energy into hydrogen energy.[1]

PEC systems, typically consisting of a photocathode and a photoanode, are capable of utilizing solar energy to split water into hydrogen and oxygen, providing a cleaner and more sustainable energy source (Fig. 1).[2,3] These systems are scalable and adaptable to various energy demands, from small-scale applications to large-scale industrial usage. PEC systems also possess the potential for high energy conversion efficiencies as they directly convert sunlight into chemical energy utilizing semiconductor materials. However, there are still many hurdles for the commercialization of green hydrogen produced by PEC systems.[4] Existing PEC systems face challenges in achieving high efficiency due to several factors related to semiconductor material properties and poor reaction kinetics.[5–7] Finding photocatalysts that are highly efficient, durable, and low cost remains a challenge, and system complexity requires expertise in multiple disciplines. Addressing these challenges, including enhancing efficiency and reducing costs through research and development, is crucial for the wide application of PEC systems as a sustainable energy solution.

In this review, we specifically discuss doping strategies of hematite (α-Fe_2O_3) photoanodes which are broadly used to improve their poor conductivity for efficient PEC water splitting systems. Particularly, we explore the effects of Sn doping caused by the thermal diffusion from the fluorine-doped tin oxide (FTO) bottom substrate under high-temperature annealing conditions. Additionally, we introduce the research trends of doping exhibiting the synergistic effects between unintentional dopant Sn and various other dopants in a multi-dopant system.

2. PEC background

2.1 Basic principle of PEC water oxidation

This review covers the simple photoelectrochemical (PEC) water splitting system, where a photoanode and a metal counter electrode are connected through an electric circuit, as illustrated in Fig. 1.[8] The PEC water splitting process involves four key steps: light absorption, charge separation, charge transfer (injection), and surface reaction. During the light absorption step, the photoelectrode absorbs photons with energy higher than the band gap of the material (E_g), which generates photoexcited carriers (h^+ and e^-). Once these carriers are generated, it becomes essential to separate them promptly to avoid recombination. Specifically, the photogenerated carriers (e^-/h^+) migrate from the bulk region to the surface of the electrodes. Subsequently, they diffuse to the solid–electrolyte

School of Energy and Chemical Engineering, Department of Energy Engineering, School of Carbon Neutrality, UNIST, Ulsan 44919, Republic of Korea. E-mail: clau@unist.ac.kr

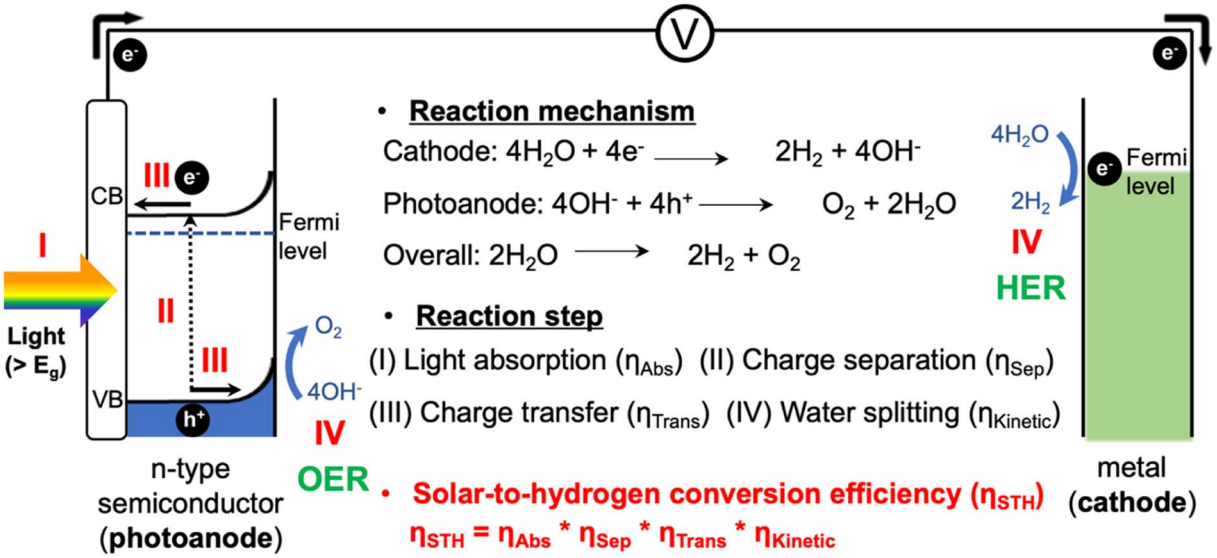

Fig. 1 Schematic illustration of the basic principle of the PEC water splitting system.

interface, initiating the water splitting reaction. At the surfaces of the photoanode and metal cathode, the oxygen evolution reaction (OER): $4OH^- + 4h^+ \rightarrow O_2 + 2H_2O$, and the hydrogen evolution reaction (HER): $4H_2O + 4e^- \rightarrow 2H_2 + 4OH^-$ are initiated, respectively.[9,10]

As per recent reports, a PEC system should have a solar-to-hydrogen conversion efficiency (STH) of over 10% to achieve the benchmark efficacy necessary to meet economic needs.[11,12] Therefore, the overall STH conversion efficiency is the most practical parameter for evaluating the PEC water splitting performance, which is determined by considering these four steps, including the light absorption properties, charge separation and transfer efficiencies, and surface OER kinetics.[13]

Since these factors heavily rely on the intrinsic properties of the material, identifying the most suitable photocatalyst becomes crucial in achieving higher STH conversion efficiency.[14]

2.2 Hematite photoanode

An ideal photocatalyst must meet several requirements, including an appropriate bandgap, extended charge lifetime, excellent stability in aqueous systems, and affordability. Various n-type semiconductor materials, such as TiO_2, ZnO, WO_3, $BiVO_4$, and α-Fe_2O_3, have been extensively investigated for their unique electrochemical properties, low cost, and high stability.[15–23] Each one exhibits its own set of advantages and disadvantages as described in Table 1.

There are many challenges involved in synthesizing an ideal photocatalyst that can fulfill all the above-mentioned requirements. Therefore, to drive PEC technology towards commercial viability, it is imperative to explore a diverse range of approaches, including alloying, creating heterojunctions, and doping, to optimize the materials.[27–29]

Hematite (α-Fe_2O_3) is one of the promising photoanode candidates for PEC water splitting as it possesses an ideal bandgap for a broad range of visible light absorption, high chemical stability in alkaline electrolytes, natural abundance, and non-toxicity.[30–32] However, the practical STH conversion efficiency of hematite is far below the theoretical values (~15%) due to its short hole diffusion length (2–4 nm), low electrical conductivity, sluggish water oxidation kinetics, and inappropriate band position for water oxidation and reduction (Fig. 2a).[33,34] Note that hematite can achieve a theoretical maximum STH efficiency of 15%, which exceeds the benchmark efficiency of 10%. Despite how it may sound, there are several challenges involved in reaching the maximum theoretical STH efficiency.

Fig. 2b illustrates the differences in the performance of the ideal and actual hematite photoanode.[35] *J–V* curves represent the actual hematite photoanode with the anodic onset potential and lower photocurrent density compared to the ideal hematite photoanode primarily due to the sluggish charge transfer and poor separation efficiency of the actual hematite photoanode. Extensive research efforts have been directed towards multiple aspects, such as growing hematite on diverse substrates (*e.g.*, metal, FTO, patterned FTO), applying various modifications, including constructing junctions, doping, nanostructuring, and interfacial engineering with overlayer and underlayer coating. These endeavors aim to enhance charge separation, transfer, and surface OER (oxygen evolution reaction) kinetics, as depicted in Fig. 3.

This review primarily focuses on heteroatom-doped hematite on a fluorine-doped tin oxide (FTO) substrate and summarizes future perspectives that can lead to further advancements in this field. It offers valuable insights into the modification strategies employed and the progress achieved in terms of electronic and morphological changes through heteroatom doping. It also highlights the technical challenges associated with the α-Fe_2O_3 photoanode, which currently hinder the realization of its full potential in practical solar hydrogen production systems.

Table 1 Advantages and disadvantages of potential photoanode materials[5,6,12,24–26]

	Advantage	Disadvantage
Fe_2O_3	Earth-abundance and low cost	Short hole diffusion length (2–4 nm)
	Nontoxicity and good PEC stability	Low electron mobility ($\sim 10^{-1}$ cm^2 V^{-1} s^{-1})
	Narrow bandgap (2.0–2.2 eV)	Sluggish water oxidation kinetics
WO_3	Stable in acid conditions	Large band gap of 2.6–3.0 eV
	Moderate hole-diffusion length (~150 nm)	Photo-corrosion during PEC reaction
	Good electron mobility (~12 cm^2 V^{-1} s^{-1})	Sluggish water oxidation kinetics
ZnO	Environmentally friendly	Large bandgap of 3.2 eV
	Electron lifetime exceeding 10 s	Fast charge recombination
	High electron mobility	Insufficient surface reactivity
$BiVO_4$	Suitable bandgap of 2.4–2.5 eV	Poor electrical conductivity
	Relatively high conduction band edge	Sluggish water oxidation kinetics
	Sluggish OER kinetics	Poor chemical stability
TiO_2	Earth-abundance and high stability	Large bandgap of 3.0–3.2 eV
	Suitable valence band edge	Low absorption for visible light
	Good electrical properties	Poor charge separation

3. Heteroatom doping

3.1 Heteroatom doping and limitations

The primary aim of heteroatom doping is to modify the photocatalytic properties, such as bulk carrier concentration, conductivity, and charge separation efficacy of semiconductors, which is a widely utilized approach (Table 2). By introducing dopants into the semiconductor lattice, both the electronic and morphological properties can be enhanced to improve photocatalytic activity. In light of this, both metallic n-type and non-metallic n-type dopants, each possessing distinct photocatalytic potential, are commonly employed to enhance the performance of n-type α-Fe_2O_3.

Additionally, the incorporation of p-type dopants into metal-doped hematite is proposed as a solution to reduce the high charge recombination rate of metal-doped hematite.[44,45] This strategy aims to create extra states situated above the valence band of hematite and establish a p–n junction at the surface, efficiently mitigating charge recombination by providing an additional driving force for charge separation.[46,47]

In addition to p-type and n-type doping using dopants of various oxidation numbers, trivalent dopants such as Al^{3+} and B^{3+} can act as donor levels in hematite, increasing carrier density and potentially enhancing its efficiency for photoelectrochemical water splitting.[48] This is because trivalent dopants like Al^{3+} and B^{3+} create a higher positive charge density than the surrounding Fe atoms due to their smaller ionic size, even with the same ionic charge. Consequently, the surrounding oxygen atoms move toward the trivalent dopants because of the stronger coulombic attraction compared to Fe. This transformation in chemical bonding introduces lattice strain and ultimately reduces the overall lattice volume, which is beneficial for electron hopping.[49]

Several types of dopants play a crucial role in enhancing the PEC activities of hematite by addressing challenges such as low electron mobility (10^{-2} cm^2 V^{-1} s^{-1}) and low carrier density (10^{18} cm^3), and reducing the overpotential for hematite water oxidation.[30] Additionally, these dopants offer the ability to achieve diverse effects, including the control of morphological and optical properties.[20] As mentioned above,

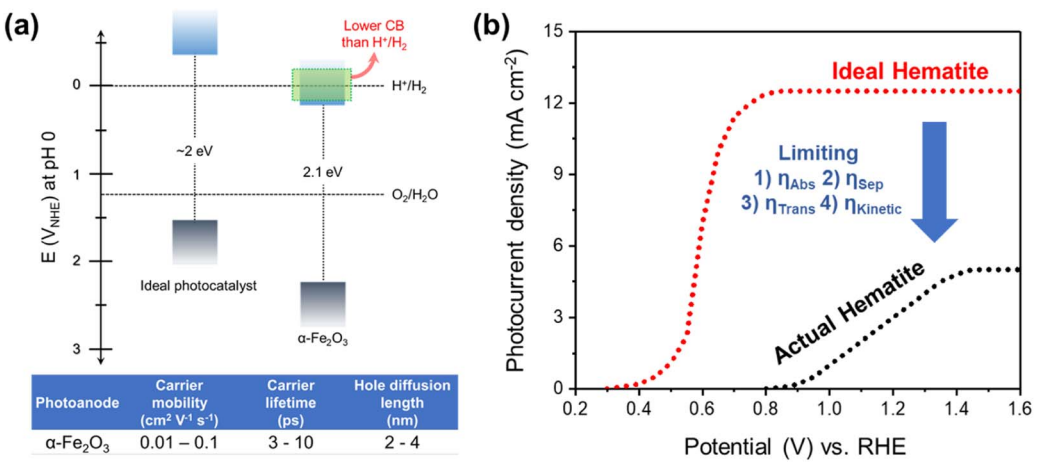

Fig. 2 (a) Band edge positions and electronic properties of hematite. (b) PEC performance of the ideal hematite photoanode and actual hematite photoanode.

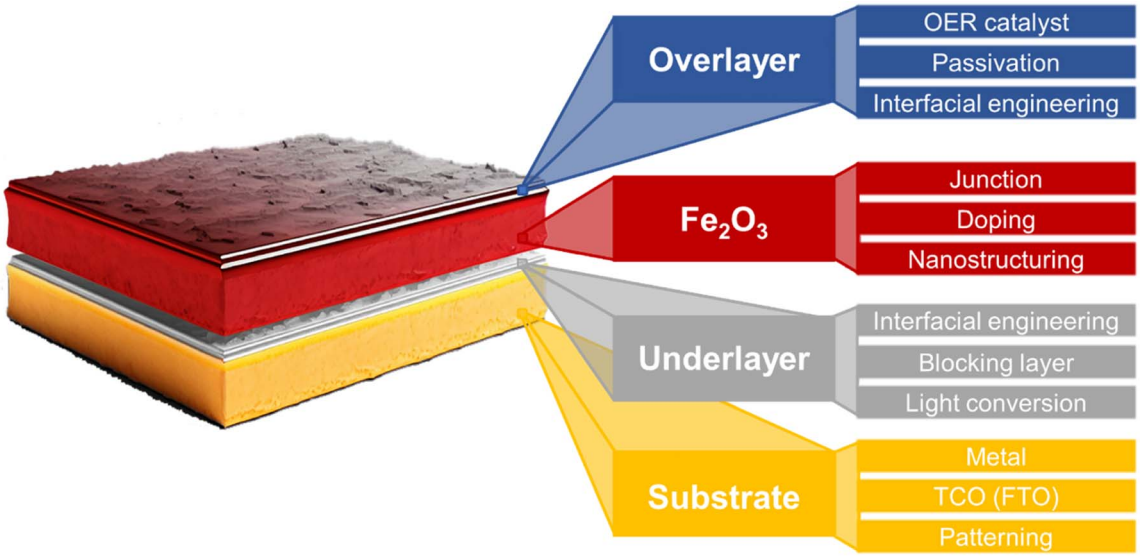

Fig. 3 Schematic illustration of various strategies for enhancing PEC efficiencies of a hematite photoanode.[35–43]

various dopants exhibit diverse characteristics, and the doping methods are critical research areas for optimizing hematite's performance. Consequently, recent research has placed its focus on various doping techniques, encompassing atomic-level doping engineering.[50,51] In this perspective article, we will delve specifically into the heteroatom doping

Table 2 Hematite photoanodes doped with different heteroatoms and PEC performance

Dopant	Photocurrent density (mA cm^{-2})	Potential *vs.* RHE	Electrolyte	Carrier density (10^{20} cm^{-3})	Year (ref.)
Ti	1.25	1.23	1 M NaOH	—	2016 (ref. 52)
Ti	0.92	1.23	1 M KOH	—	2016 (ref. 53)
P	2.70	1.23	1 M NaOH	1.01	2015 (ref. 54)
P	1.48	1.23	1 M KOH	5.80	2017 (ref. 55)
P/Ti	2.50	1.23	1 M NaOH	3.48	2023 (ref. 56)
P/Ru	4.55	1.23	1 M KOH	—	2023 (ref. 50)
Si	2.20	1.23	1 M NaOH	—	2006 (ref. 57)
Si/Ti	2.44	1.23	1 M NaOH	—	2016 (ref. 52)
Si/Ti	2.36	1.23	1 M NaOH	—	2020 (ref. 58)
Si/Ti	3.00	1.23	1 M NaOH	1.52	2022 (ref. 59)
Sn	0.56	1.23	1 M NaOH	—	2010 (ref. 60)
Sn	1.24	1.23	1 M NaOH	0.538	2011 (ref. 61)
Sn	0.98	1.23	1 M NaOH	—	2015 (ref. 62)
Sn	1.38	1.23	1 M KOH	—	2017 (ref. 63)
Sn/Be	1.70	1.23	1 M NaOH	0.803	2016 (ref. 64)
Sn/Si	3.00	1.23	1 M NaOH	2.90	2021 (ref. 65)
Ge	1.40	1.23	1 M NaOH	0.302	2014 (ref. 66)
Ge	3.50	1.23	1 M NaOH	3.10	2021 (ref. 67)
B	~0.1	1.23	1 M NaOH	—	2018 (ref. 44)
B/Ti	1.92	1.23	1 M NaOH	8.50	2018 (ref. 44)
Mg	~0.5	1.23	1 M KOH	—	2012 (ref. 47)
Mg	0.763	1.23	1 M NaOH	41.1	2022 (ref. 45)
Mg/P	2.4	1.23	1 M NaOH	2.97	2018 (ref. 46)
Al	~0	1.23	1 M NaOH	0.02	2014 (ref. 68)
Al/Ti	1.30	1.23	1 M NaOH	1.70	2014 (ref. 68)
Zr	1.50	1.23	1 M KOH	5.88	2017 (ref. 69)
Ta	1.93	1.23	1 M NaOH	—	2020 (ref. 70)
Ta/Sn	2.37	1.23	1 M NaOH	—	2019 (ref. 71)
Pt	2.19	1.23	1 M NaOH	0.0277	2013 (ref. 72)
Pt	2.71	1.23	1 M KOH		2023 (ref. 51)
Nb	0.63	1.00	0.5 M Na_2SO_4	9.42	2016 (ref. 73)
Nb/Sn	1.88	1.23	1 M KOH	0.321	2019 (ref. 74)
Gd	~1.5	1.23	1 M KOH	0.0217	2022 (ref. 32)

method, particularly involving surface overlayers, among the array of available approaches.

3.1.1 Phosphorus doping. The utilization of non-metallic dopants with covalent characteristics, forming strong bonds with the oxygen atoms in hematite, shows great potential in enhancing its electronic properties. This approach enables the introduction of additional electrons to the Fe ions, resulting in a significant improvement in the photoelectrochemical (PEC) performance. Kang *et al.* demonstrated an *in situ* non-metal phosphorus (P) doping method on the Ti-doped Fe_2O_3 (P,Ti-Fe_2O_3) photoanode with a pore generation mechanism by utilizing a thin $FePO_4$ overlayer coated on Ti-FeOOH nanorods.[56]

Fig. 4a shows the X-ray photoelectron spectroscopy (XPS) depth profile for P/Fe of P,Ti-Fe_2O_3, which revealed evidence of P doping from the surface overlayer to the hematite lattice. Due to the P doping effect, P,Ti-Fe_2O_3 exhibited a shift of an O 1s peak towards higher binding energy, indicating the presence of oxygen atoms bonded with phosphorus (Fig. 4b). This led to an enhanced carrier density of P,Ti-Fe_2O_3 compared to that of Ti-Fe_2O_3 (Fig. 4c). The band structure analysis confirmed the band shift resulting from the injection of P (Fig. 4d) and revealed that the gradient P doping facilitated more efficient charge transport by creating an internal electric field (Fig. 4e). In *J–V* curves, P,Ti-Fe_2O_3 exhibited a photocurrent density of 2.5 mA cm^{-2} at 1.23 V_{RHE}, which was a 94% improvement compared to that of a Ti-Fe_2O_3 photoanode as shown in Fig. 4f. The formation of a pore structure holds great importance in hematite, which greatly suffers from the very short hole diffusion length (2–4 nm) issue. This highlights the significance of the pore generation method. In addition to the alterations in electronic properties, the *in situ* P doping method created a mesoporous nanorod structure of P,Ti-Fe_2O_3 with much shortened diffusion pathways (Fig. 4h), different from the conventional wormlike structure of Ti-Fe_2O_3 (Fig. 4g). The pore generation occurred as a result of water evaporation in the P,Ti-FeOOH nanorod within the $FePO_4$ hard template during the high-temperature dehydration process, which created vacancies.

The synthesis development of porous hematite, along with doping, has also offered a new opportunity to overcome the limited efficacy of the hematite photoanode. A porous structure improves solar energy conversion by (i) enhancing light scattering, (ii) facilitating an electron transfer pathway, and (iii) increasing the specific surface area. In 2016, Jang *et al.* reported a synthesis mechanism for porous hematite on an FTO surface.[52] In the conventional hematite synthesis method, the high-temperature conditions caused Ti-FeOOH nanorods to coalesce, resulting in a worm-like, non-porous structure of Ti-Fe_2O_3 (Fig. 5b). On the other hand, to create a nanoporous hematite structure, they employed a Ti-doped amorphous SiO_x overlayer on Ti-FeOOH. With the Ti-doped SiO_x overlayer, the grain boundary motion appeared to occur inwards within each rod, accompanied by the evolution of HCl and H_2O gases under the rigid SiO_x overlayer through the dehydration process. Thus, Ti-doped SiO_x overlayer coated hematite exhibited numerous pores (Ti-(SiO_x/np-Fe_2O_3)) in the core and thick frames in the shell (Fig. 5c). The uniform distribution of Si atoms was confirmed through EDS mapping images (Fig. 5d) and XPS analysis (Fig. 5e). As a result of the nanoporous structure formation and the passivation effect of the SiO_x overlayer on Ti-(SiO_x/np-Fe_2O_3), the Ti-(SiO_x/np-Fe_2O_3) photoanode exhibited an improved photocurrent density of 2.44 mA cm^{-2} at 1.23 V_{RHE} (Fig. 5f). Through the development of doping methods using surface overlayer coating, not only heteroatom doping but also the fabrication of a nanoporous structure became easily achievable.

3.1.2 Silicon doping. The primary aim of heteroatom doping in hematite is to alter its electrical properties. However, this process is limited by the structural distortion caused by the size difference and strong repulsion between different types of dopants. Therefore, it is important to understand the interactions among dopants. Yoon and co-workers focused on the interactions between two dopants (Sn^{4+} and Ti^{4+}) in terms of formation energy, related to crystal disorder, with the aid of density functional theory (DFT) calculations.[59] Using conventional hydrothermal methods and high-temperature annealing processes of the corresponding precursor materials with a SiO_x overlayer, they fabricated Si-doped Fe_2O_3 (Si-Fe_2O_3) and Si and Ti-co-doped Fe_2O_3 (Si:Ti-Fe_2O_3) with similar porous structures but different Ti concentration (Fig. 6a–c). To demonstrate the Si doping of Si-Fe_2O_3 and Si:Ti-Fe_2O_3 through thermal diffusion from the SiO_x overlayer to the hematite lattice, they conducted a 3D time-of-flight secondary ion mass spectrometry (TOF-SIMS) analysis. Fig. 6d shows that Si was diffused into the hematite lattice in Si:Ti-Fe_2O_3 after annealing SiO_x/Ti-FeOOH, which was further supported by XPS depth profiles in Fig. 6e. High-magnification bright-field TEM images showed that Si-Fe_2O_3 had a 2–3 nm-thick amorphous region in the outer surface after the SiO_x layer was etched, which suggested structural disorder induced by Si diffusion (Fig. 6f), which was due to the smaller ionic radius of Si^{4+} (40 pm) compared to that of Fe^{3+} (55 pm). On the other hand, by balancing the ionic radius with the larger atom Ti^{4+} (66.5 pm), only a 1 nm or less thick outer surface amorphous region was identified in Si:Ti-Fe_2O_3 after etching the SiO_x layer (Fig. 6g). The higher structural disorder of Si-Fe_2O_3 compared to Si:Ti-Fe_2O_3 was also verified by DFT calculations in Fig. 6h and i. When Si and Ti dopants were together in the hematite lattice, the binding energy of Si–O was lower, making simple solution-based Si-doping possible. The synergistic effect of Si and Ti dopants was confirmed using *J–V* curves in Fig. 6j, implying that the positive interaction between dopants is essential not only for the thermodynamic stability of the photoanode but also for enhanced water splitting properties.

3.1.3 Sn doping. The systematic investigation of the Sn doping effect is important because Sn unintentionally diffuses from the FTO substrate during the high-temperature annealing process, which is common in the fabrication of the hematite photoanode. Conventionally, α-Fe_2O_3 is fabricated through a two-step process: first, hydrothermally growing β-FeOOH nanorods on the FTO substrate, and then performing thermal annealing.[67] High-temperature annealing, commonly exceeding 700 °C, is frequently used to enhance the PEC performance of hematite through Sn diffusion doping utilizing a bottom-up

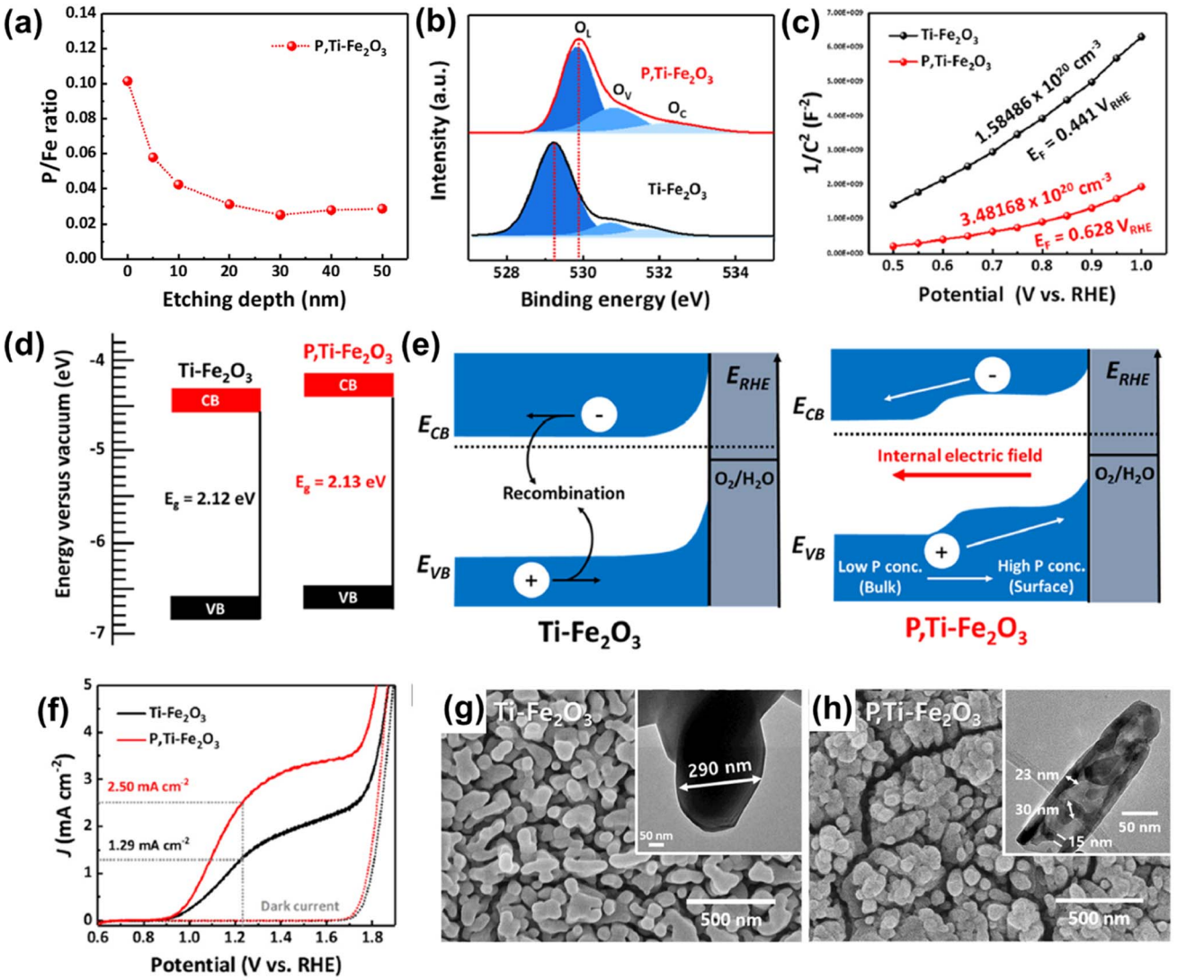

Fig. 4 (a) XPS depth profiles for P/Fe of P,Ti-Fe_2O_3. (b) XPS O 1s spectra of Ti-Fe_2O_3 and P,Ti-Fe_2O_3. (c) Mott–Schottky plots at a frequency of 1 kHz. (d) Band diagrams and (e) band edge positions of Ti-Fe_2O_3 and P,Ti-Fe_2O_3 photoanodes. (f) J–V curves for Ti-Fe_2O_3 and P,Ti-Fe_2O_3 under 1 sun and dark conditions in a three-electrode system. SEM image of (g) Ti-Fe_2O_3, and (h) P,Ti-Fe_2O_3 (insets in (g) and (h) show TEM images of Ti-Fe_2O_3 and P,Ti-Fe_2O_3). Reproduced from ref. 56 with permission from Elsevier, Copyright 2023.

approach, and promoting increased crystallinity.[62,75] Sivula *et al.* investigated the effect of Sn^{4+} doping on hematite by the thermal diffusion of Sn from the FTO substrate to the hematite lattice.[60] Hematite electrodes prepared using a solution-based colloidal method and annealed at 800 °C demonstrated a notable increase in photocurrent density due to the electronic modification of mesoporous film caused by the incorporation of Sn^{4+} from the FTO substrate during the annealing process compared to hematite electrodes that were annealed at lower temperature (Fig. 7a). The presence of distinct Sn intensity in the hematite electrode annealed at 800 °C confirmed the Sn doping (Fig. 7b). In addition, the high photocurrent density observed in the hematite electrode annealed at 800 °C was also attributed to the larger average particle size and higher light absorption properties, in comparison to other hematite samples shown in Fig. 7c and d.

A more detailed study of Sn diffusion from the FTO substrate into hematite was carried out by Annamalai *et al.*, where they reported that Sn acted as an n-type dopant.[62] Depending on the annealing time (at 800 °C for 2, 10, and 20 min), different amounts of Sn in the FTO substrate were diffused into the hematite lattice. A sudden decline in photocurrent was observed in hematite nanorods sintered for 20 min (Fig. 8a). This was attributed to the significant amount of diffused Sn content exceeding 3% in hematite, consequently causing the deformation of the FTO substrate and increasing resistivity due to changes in the stoichiometry of the FTO substrate. To investigate FTO deformation caused by excess Sn diffusion, the Fourier-transformed spectra of extended X-ray absorption fine structure (EXAFS) analysis were examined for the Sn K-edge of the FTO substrate (Fig. 8b). The intensity of the peak in the region of 0.8 to 2.0 Å,

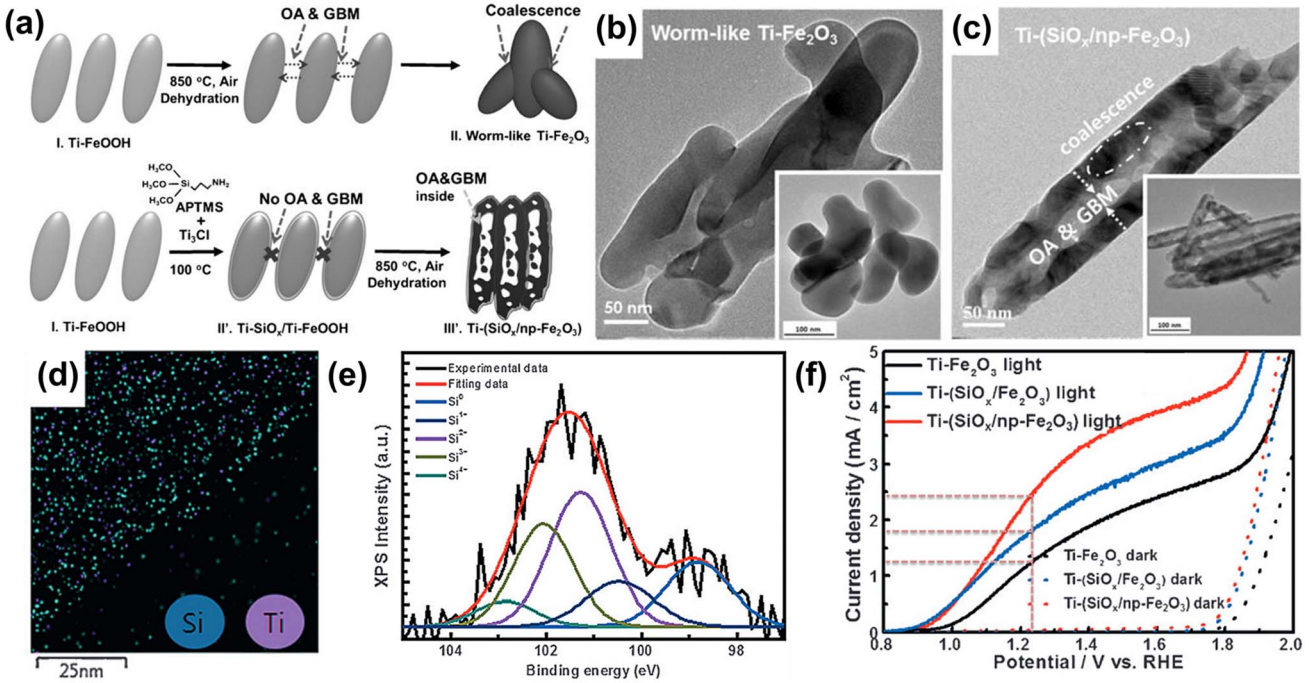

Fig. 5 (a) The fabrication procedures for conventional worm-like Ti-Fe_2O_3 and Ti-(SiO_x) layer-coated porous hematite (Ti-(SiO_x/Fe_2O_3)). TEM image of (b) a worm-like Ti-Fe_2O_3 and (c) Ti-(SiO_x/np-Fe_2O_3). (d) EDS mapping images of Si and Ti of Ti-(SiO_x/np-Fe_2O_3). (e) XPS Si 2p spectra of Ti-(SiO_x/np-Fe_2O_3). (f) *J*–*V* curves of Ti-Fe_2O_3, Ti-(SiO_x/Fe_2O_3), and Ti-(SiO_x/np-Fe_2O_3) under 1 sun and dark conditions with a three-electrode system. Reproduced from ref. 52 with permission from Wiley-VCH, Copyright 2016.

corresponding to short Sn–O bonding, followed the sequence 20 min < 0 min ≈ 2 min < 10 min, implying enhanced ordering with an increase in Sn diffusion up to 10 min of annealing. Due to a trade-off between Sn diffusion into the hematite lattice and loss of Sn in the FTO substrate, applying optimized annealing conditions with moderate Sn diffusion minimized the deformation of FTO, leading to high PEC activities. Based on these findings, they concluded that Sn doping had a positive impact, particularly when performed at an optimal sintering time of 10 minutes. This resulted in achieving the highest photocurrent density of 0.98 mA cm^{-2} at 1.23 V_{RHE}. The study emphasized the significance of controlling the Sn diffusion from the FTO substrate, as it influenced various factors including charge recombination centers, structural disordering, and electrical conductivity of both the photoanode and the substrate.

3.1.4 Controlling Sn diffusion from the FTO substrate through intentional Sn doping. In general, hematite fabrication on an FTO substrate takes place under high-temperature annealing. Consequently, Sn from the FTO substrate commonly diffuses into the hematite layer. This unintentional diffusion of Sn is often associated with enhancements in PEC activity. However, excessive Sn diffusion has been found to cause structural disorder, resulting in lower PEC activity. Understanding and distinguishing the exact roles of each dopant, whether unintentionally or intentionally incorporated, is quite challenging in this field. In light of this, controlling unintentional Sn diffusion is a crucial step in hematite fabrication.

Li *et al.* developed a method to control unintentionally diffused Sn and further enhance the Sn diffusion effects from the FTO substrate obtained by a bottom-up approach.[63] They observed that while Sn enhances the PEC performance of hematite, the amount of Sn diffusing from the bottom is limited. Moreover, the high-temperature treatment required for Sn diffusion was found to cause structural deformation. To address these issues, they utilized a top-down method for Sn diffusion, decorating an additional Sn precursor on the surface of hematite to increase Sn concentration. They also encapsulated the hematite nanowires with silica through thermal diffusion. Compared to the normal hematite nanowire (Sn-Fe_2O_3) with unintentional Sn content diffused from the bottom FTO substrate, which also substantially shrank after high-temperature annealing, the one synthesized by drop-casting a Sn precursor and encapsulating it with a silica shell exhibited robust characteristics under the high-temperature annealing (800 °C) process (Fig. 9a). This resulted in a morphology-and-doping-engineered hematite nanowire (E-I-Sn-Fe_2O_3). By silica encapsulation and the addition of a Sn precursor before high-temperature annealing, E-I-Sn-Fe_2O_3 retained its morphology while improving the uniformity of dopant distribution along the nanowire growth axis as shown in XPS spectra and SIMS depth profiles in Fig. 9b and c. The high Sn concentration at the first 100 nm of E-I-Sn-Fe_2O_3 may arise from the uneven deposition of the Sn precursor onto the densely arranged NW arrays. They claimed that the enhanced photocurrent density and IPCE of the E-I-Sn-Fe_2O_3 are due to retaining the nanowire morphology and uniform

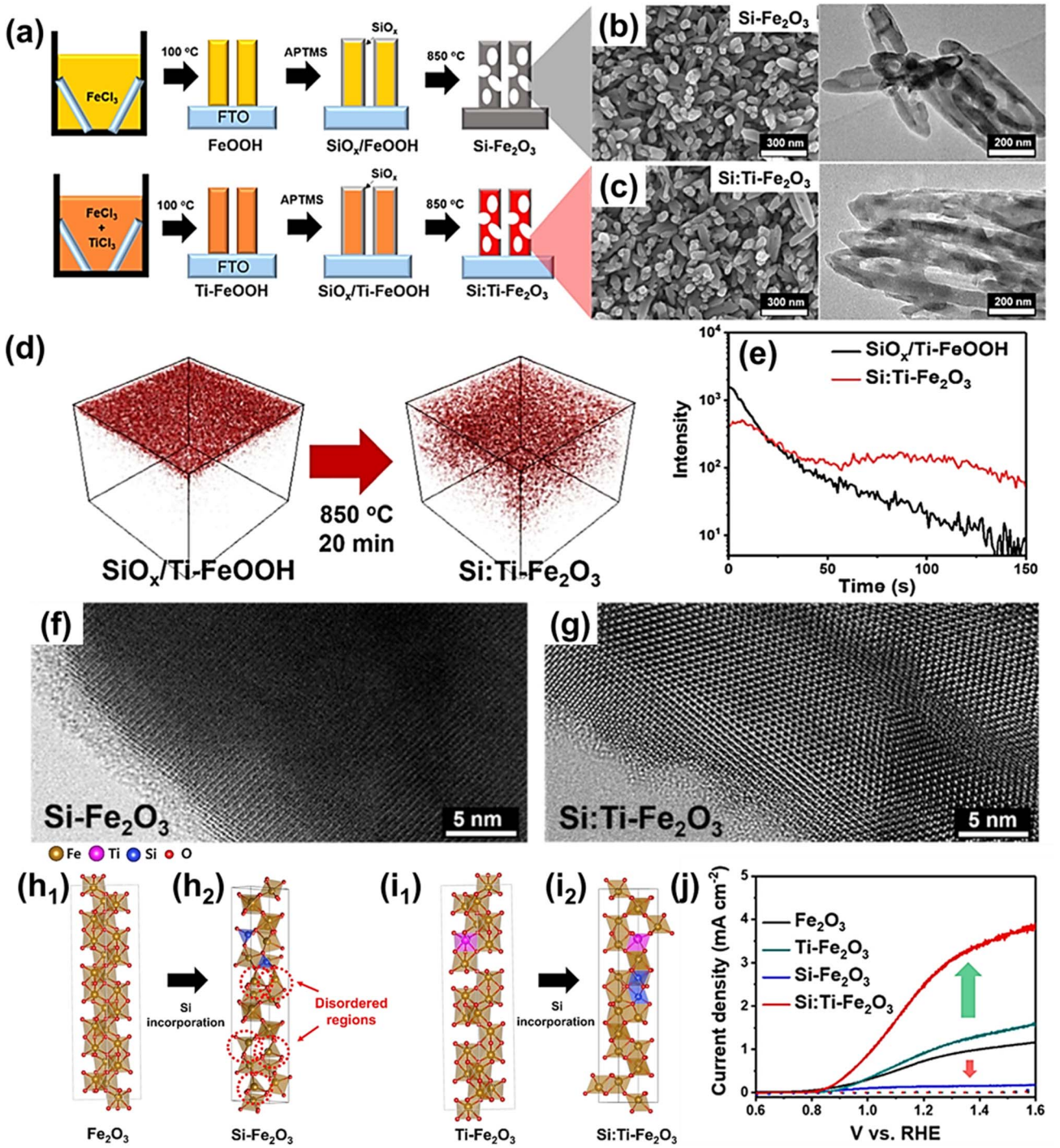

Fig. 6 (a) Scheme for photoanode fabrication with the SiO_x layer w/wo the host Ti-dopant. Transmission electron microscopy (TEM) and scanning electron microscopy (SEM) images for (b) Si-Fe_2O_3 and (c) Si:Ti-Fe_2O_3. (d) Three-dimensional TOF-SIMS Si distribution before (SiO_x/Ti-FeOOH film) and after (Si:Ti-Fe_2O_3 film) annealing and (e) TOF-SIMS depth profiles for Si distribution. High-magnification bright-field TEM images of (f) Si-Fe_2O_3 and (g) Si:Ti-Fe_2O_3 after etching the SiO_x layer. (h) Atomic structures without host Ti-dopants for (h_1) Fe_2O_3 and (h_2) Si-Fe_2O_3. (i) Atomic structures with host Ti-dopant for (i_1) Ti-Fe_2O_3 and (i_2) Si:Ti-Fe_2O_3. (j) J–V curves of Fe_2O_3, Ti-Fe_2O_3, Si-Fe_2O_3, and Si:Ti-Fe_2O_3. Reproduced from ref. 59 with permission from American Chemical Society, Copyright 2022.

distribution of Sn (Fig. 9d and e). This study presents the effects of intentional Sn doping on the morphology and doping uniformity to control unintentionally diffused Sn from the FTO substrate and assess its influence on the photoelectrochemical (PEC) performance of hematite photoanodes.

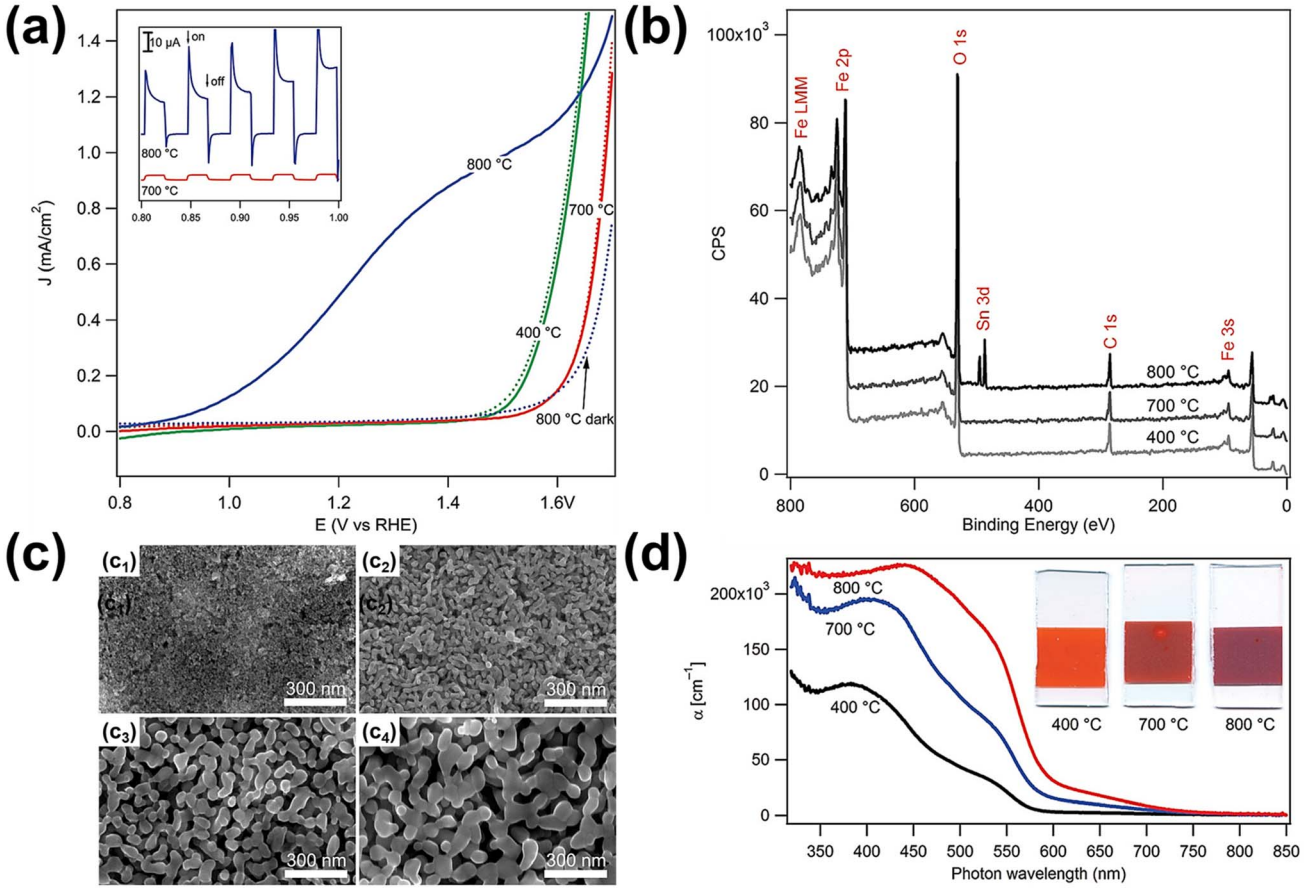

Fig. 7 (a) Electrochemical water oxidation current *vs.* voltage curves of the photoanodes sintered at different temperatures in the dark (dotted curves) and under simulated solar light (solid curves, AM 1.5G 100 mW cm^{-2}, spectrally corrected). The inset shows the photocurrent transient curves for the 700 and 800 °C samples created by chopping the light source during a current *vs.* voltage sweep. (b) X-ray photoelectron spectroscopy survey data for the electrodes sintered at different temperatures. (c) Scanning electron micrographs of mesoporous hematite films prepared on SiO_2/F:SnO_2 substrates after different heat treatments: (c_1) as deposited with a porogen, (c_2) after 10 h at 400 °C, and (c_3) after 20 min at 700 °C and (c_4) 800 °C. (d) Absorption coefficient as a function of wavelength and the typical appearance of the electrodes (25 mm height, all derived from the same parent substrate). Reproduced from ref. 60 with permission from American Chemical Society, Copyright 2010.

3.2 Multiple dopants (B, Si, Ti, and Ge) for controlling metal dopants of Fe_2O_3 (unintentionally diffused Sn)

The positive effect of Sn diffusion from the FTO substrate into the hematite lattice is described in the previous section. In more advanced co-doping systems, the role of Sn diffused from the FTO substrate may be quite different. There have been several reports that Sn doping can induce negative effects even under the doping limit when multiple heteroatoms are doped into the hematite lattice due to bad interaction among different atoms. Therefore, material design with theoretical validation should be carefully studied, so that material synthesis close to the designed system can be approached more scientifically. In this section, we introduce several reports on the hematite photoelectrochemical effects with controlled Sn content at the surface region where the recombination should be carefully considered to boost the OER properties.

3.2.1 Boron doping. To achieve higher photoelectrochemical efficiency of hematite photoanodes, many reports have investigated the control of Sn diffusion from the FTO substrate through the utilization of various dopants, such as boron (B), silicon (Si), and germanium (Ge). Ahn *et al.* reported an effective approach to control the content of metal dopants (Ti^{4+} and Sn^{4+}) in hematite through the use of non-metallic B doping.[44] Boron doping was achieved by simply dipping M-doped FeOOH in a boric acid solution, followed by heat treatment at 800 °C. The incorporation of B ions in M-doped hematite not only decreased the number of Ti and Sn ions responsible for electron–hole pairs recombination at the hematite surface but also generated an internal electric field that facilitated easy hole extraction, as shown in the schematic illustration in Fig. 10a. The B doping was revealed by XPS B 1s spectra in Fig. 10b. The enhanced photocurrent density (Fig. 10c) and higher IPCE values in a range from 300 to 550 nm at 1.23 V_{RHE} (Fig. 10d) clearly show the synergetic effect of the reduced recombination due to a decreased number of Sn^{4+} ions at the surface of M:B-Fe_2O_3 (Fig. 10e) and the creation of an internal electric field by an n–n$^+$ junction. This work introduced a mitigating strategy of metal-doping-related negative effects by non-metallic boron doping.

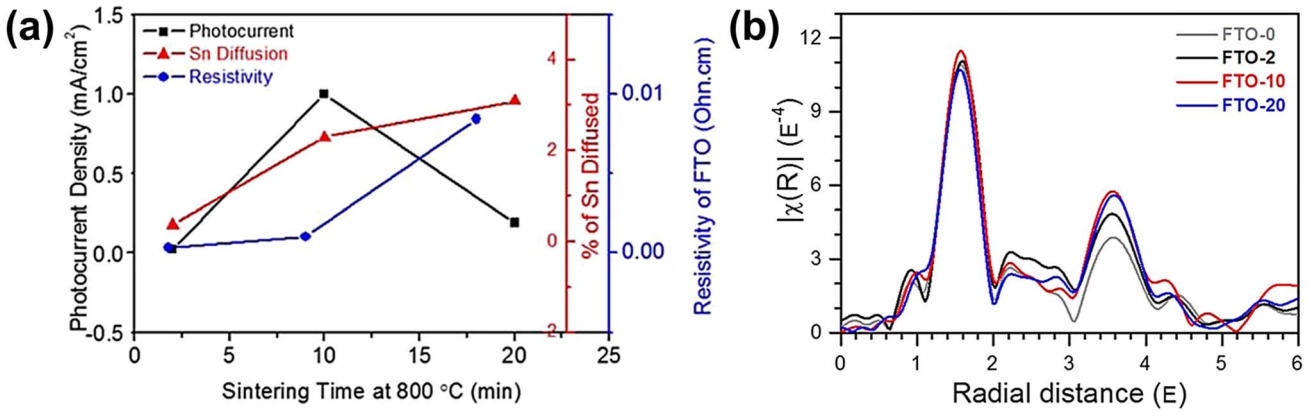

Fig. 8 (a) Photocurrent density (mA cm^{-2}), atomic percent of Sn diffusion of hematite photoanodes, and resistivity of the FTO substrate sintered at 800 °C for 2, 10, and 20 min. k^3-weighted Fourier transforms for (b) Sn K-edge EXAFS of FTO substrates sintered at 800 °C for 0, 2, 10, and 20 min. Reproduced from ref. 62 with permission from American Chemical Society, Copyright 2015.

3.2.2 Silicon doping. Ion mobility tends to increase with increasing temperature over the same time frame as changes in crystallinity. Taking this into consideration, Park *et al.* investigated the limit of Sn diffusion length.[58] They employed non-metallic Si-doping to regulate the Sn concentration at the surface region of hematite photoanodes. In order to enhance the transparency of the hematite photoanode and minimize optical losses of a solar cell in hematite/perovskite tandem cell systems, they fabricated a very thin Ti-doped hematite film (70 nm, Ti-Fe_2O_3(t)) but observed lowered photocurrent density. They paid attention to the Sn content at the surface region of the photoanode where the OER reaction takes place. They hypothesized that the relatively lower PEC efficiency of Ti-Fe_2O_3(t) compared to a conventional thick Ti-doped hematite film (350 nm, Ti-Fe_2O_3(T)) was mainly attributed to an excessive concentration of metal dopants (Sn) at the surface region diffused from the bottom FTO substrate in the thin film case (Fig. 11a). In order to address this issue, they employed non-metallic Si doping on the thin film of Ti-Fe_2O_3(t) (Ti:Si-Fe_2O_3(t)) by introducing a SiO_x overlayer onto Ti-FeOOH before heat treatment. The atomic arrangement of Ti-Fe_2O_3(t) and Ti:Si-Fe_2O_3(t) is illustrated in the schematic diagram (Fig. 11b). The introduction of silicon through the overlayer resulted in Si diffusion from the hematite surface, significantly suppressing the diffusion of Sn from the bottom substrate. The XPS spectra revealed a distinct Si peak (Fig. 11c) and a decreased Sn^{4+} peak

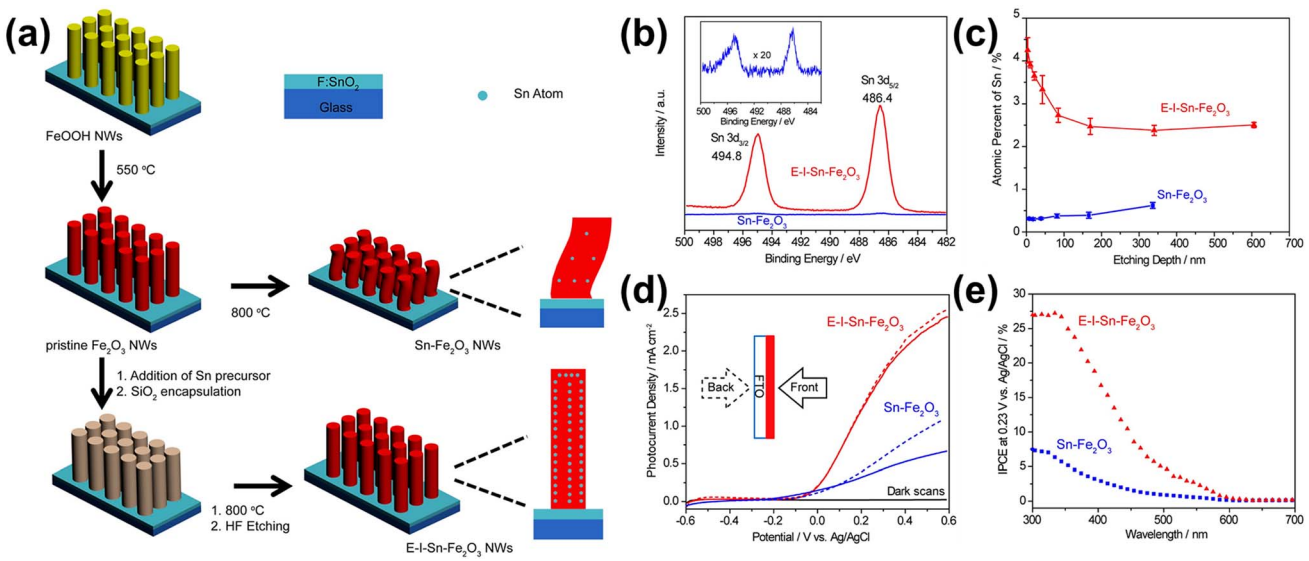

Fig. 9 (a) Schematic illustration of the preparation of Sn-Fe_2O_3 NWs and E-I-Sn-Fe_2O_3 NWs. (b) XPS Sn 3d spectra of Sn-Fe_2O_3 and E-I-Sn-Fe_2O_3. Inset: magnified Sn 3d spectrum of Sn-Fe_2O_3. (c) SIMS depth profiles of Sn-Fe_2O_3 and E-I-Sn-Fe_2O_3. Error bars are evaluated based on parallel experiments. (d) J–V curves of Sn-Fe_2O_3 and E-I-Sn-Fe_2O_3 collected at 20 mV s^{-1} in a 1.0 M KOH aqueous electrolyte under one sun illumination (100 mW cm^{-2}) and in the dark. The solid and dashed lines represent the data collected under the front (solid lines) and back (dashed lines) illuminations, respectively. (e) IPCE spectra of Sn-Fe_2O_3 and E-I-Sn-Fe_2O_3 collected at 0.23 V *vs.* Ag/AgCl. Reproduced from ref. 63 with permission from American Chemical Society, Copyright 2017.

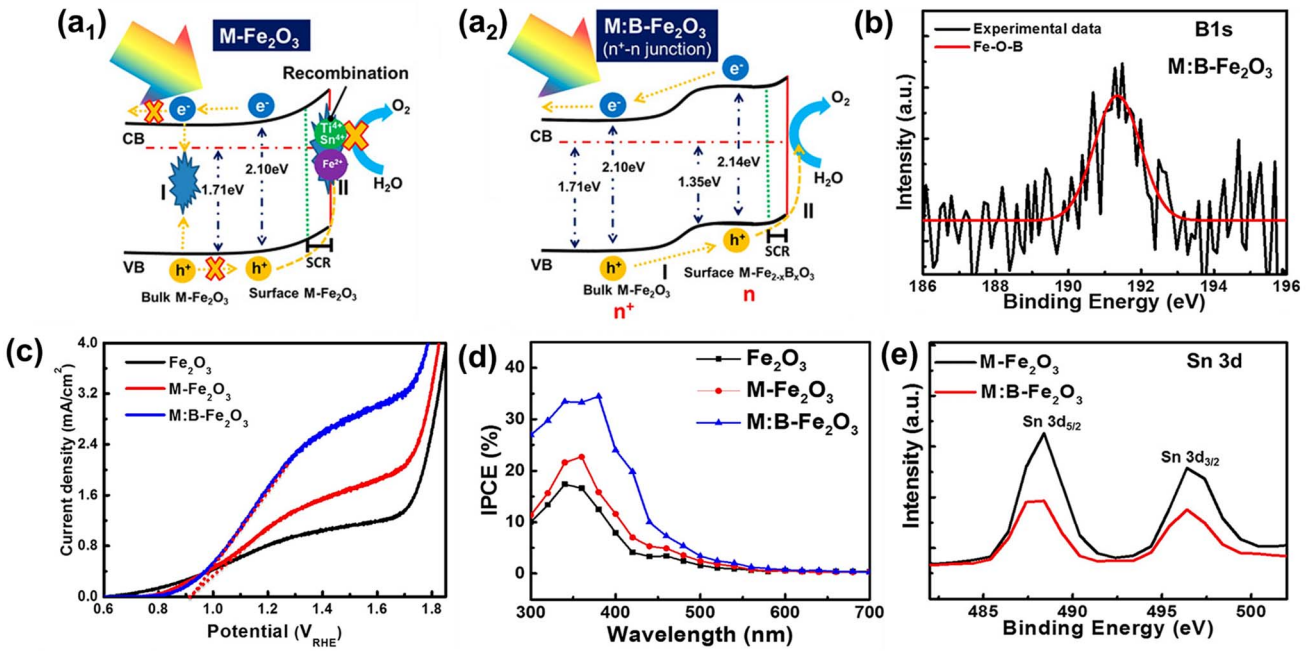

Fig. 10 (a) Schematic illustration of an energy band diagram and charge transfer process of (a_1) M-Fe_2O_3 and (a_2) M:B-Fe_2O_3, (b) XPS B 1s spectra, (c) *J*–*V* curves, (d) IPCE, and (e) XPS Sn 3d spectra. Reproduced from ref. 44 with permission from American Chemical Society, Copyright 2018.

(Fig. 11d) in Ti:Si-Fe_2O_3(t) compared to Ti-Fe_2O_3(t), which demonstrated the successful Si doping and reduction in Sn dopant concentration. By these modulations, Ti:Si-Fe_2O_3(t) showed better photoelectrochemical activities over Ti-Fe_2O_3(t), which was further confirmed by the transient photocurrent density curve in Fig. 11e. Based on these results, they argued

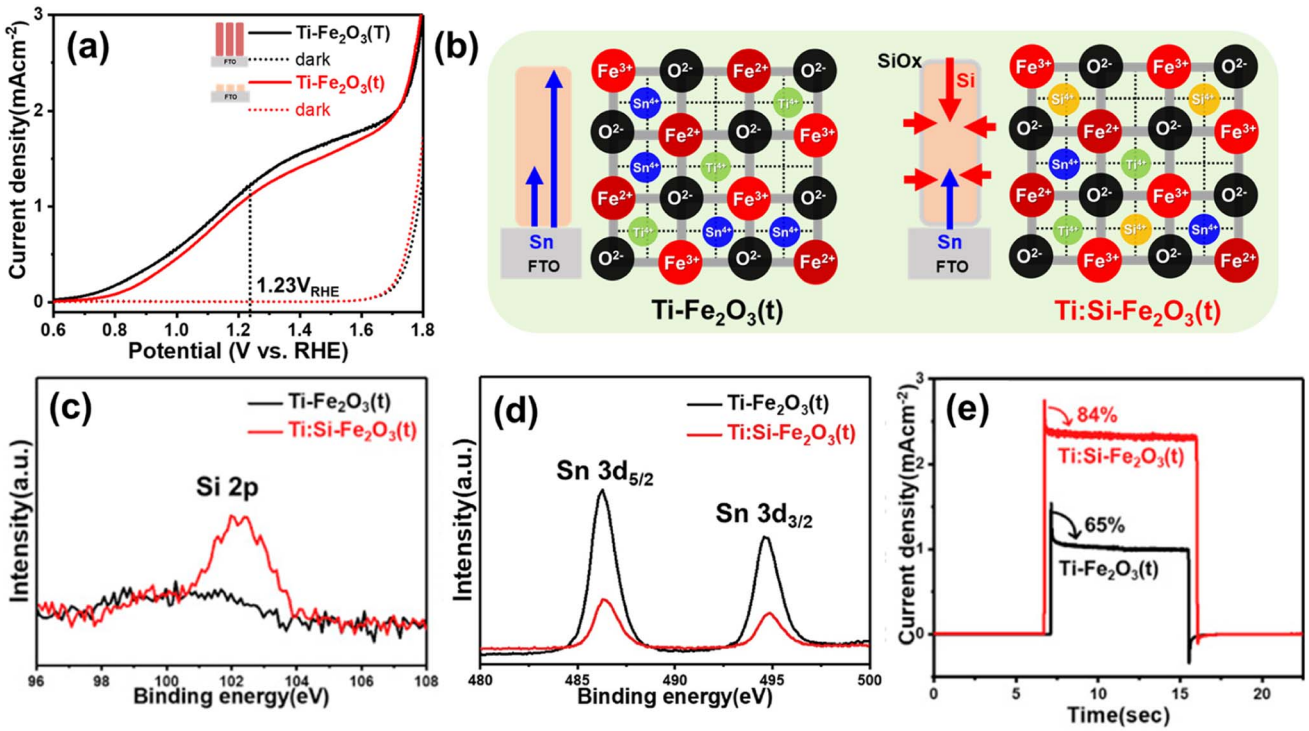

Fig. 11 (a) *J*–*V* curves of Ti-Fe_2O_3(T) and Ti-Fe_2O_3(t) under 1 sun and dark conditions. (b) Schematic diagram of decreased metal dopants (Sn^{4+} and Ti^{4+}) through non-metallic Si doping in Ti:Si-Fe_2O_3(t). XPS spectra of (c) Si 2p, and (d) Sn 3d. (e) Transient photocurrent density curves (0.001 point per s) measured at 1.23 V_{RHE} of Ti-Fe_2O_3(t), and Ti:Si-Fe_2O_3(t). Reproduced from ref. 58 with permission from Elsevier, Copyright 2020.

that the replacement of unintentionally diffused Sn by other outstanding dopants can be beneficial for better PEC performance.

To further reveal these assumptions, they developed a two-step annealing process that enables systematic control of Si and Sn content.[65] In the case of the conventional one-step annealed SiO_x overlayer-coated hematite (A-1 step, Fig. 12a), the diffusion of Sn from the FTO substrate to the hematite surface was regulated by the thickness of the SiO_x overlayer film during prolonged thermal energy exposure, as reported before.[58] In contrast, a two-step annealing method (B-1 and B-2 steps, Fig. 12a) allowed precise control over the overall amount of Sn released from the substrate by managing the diffusion length of Sn towards the surface region. In the B-1 step, Sn doping occurred only in the bulk region due to the reduced diffusion length during a short annealing time. Subsequently, in the B-2 step, the thermal diffusion of Sn from the bottom was significantly hindered, resulting from the strong binding energy between the Sn atoms, which were pre-occupied by the diffusion process during the B-1 step, and the O atoms in the bulk region. As a result, the Sn content in the surface region was more controlled, allowing for intentional Si doping to readily take place at the surface region. The different concentrations of the dopant in Sn:Si-Fe_2O_3/1 (made by one-step annealing, high Sn and low Si) and Sn:Si-Fe_2O_3/2 (made by two-step annealing, low Sn and high Si) were confirmed by XPS depth profiles in Fig. 12b and c. The reduced surface charge trapped holes and enhanced charge-transfer efficiencies of Sn:Si-Fe_2O_3/2 compared to Sn:Si-Fe_2O_3/1 were confirmed using the Nyquist plot in Fig. 12d. In the result, Sn:Si-Fe_2O_3/2 illustrated a higher photocurrent density of 2.3 mA cm^{-2} at 1.23 V_{RHE} due to the excellent OER activity of Si over Sn (Fig. 12e) at the surface region. The results provided a pathway for designing an optimal doping system with a targeted concentration of Si and Sn by manipulating the annealing process.

3.2.3 Germanium doping. According to the previous theoretical studies on hematite dopants, Ge has been reported as the best dopant due to its ability to enhance donor density while maintaining the crystallinity of hematite. This is because the ionic size of Ge^{4+} (54 pm) is similar to that of Fe^{3+} (55 pm),[59,67] which results in an outstanding solubility in hematite.[28,66] However, Yoon *et al.* found that when Ge was near Sn, the atomic structure of Ge and Sn co-doped hematite (Ge:Sn-Fe_2O_3) was thermodynamically unstable with structure disorder as shown in DFT calculation data (Fig. 13a).[67] The atomic arrangement in Fig. 13b illustrates the structural distortion caused by Sn doping and the bad interaction between Sn and Ge due to the strong charge repulsion. To experimentally confirm this, they prepared two types of Ge-doped hematite: one with high Sn content (Ge-H) and the other with suppressed Sn diffusion (Ge-PH) at the surface region of hematite. Highly reduced Sn content at the Ge-PH was revealed by XPS Sn 3d spectra in Fig. 13c. The smaller longitudinal optical (LO) mode of Ge-PH compared to the others, corresponding to the peak at 660 cm^{-1} in the Raman spectra (Fig. 13d), suggests less symmetry breakdown due to reduced Sn content (reduced Sn:Ge combination) in the surface region. In addition, the Fourier transform of the EXAFS results in the *R* space in Fig. 13e supports the less structural distortion of Ge-PH compared to Ge-H, which shows a lower FT magnitude of the Fe–O and Fe–Fe bonding lengths. With controlled Sn on the hematite surface, Ge-PH showed higher PEC catalytic efficiencies compared to other samples, which were verified by Mott–Schottky plots (Fig. 13f), EIS measurements (Fig. 13g), and *J*–*V* curves (Fig. 13h). These findings highlight the significance of managing the unintentional Sn content, which negatively interacts with Ge, to achieve enhanced PEC efficiency in Ge-doped hematite photoanodes.

In this perspective, we have explored various studies focusing on enhancing the morphological and electrical properties of hematite through heteroatom doping methods. To advance the

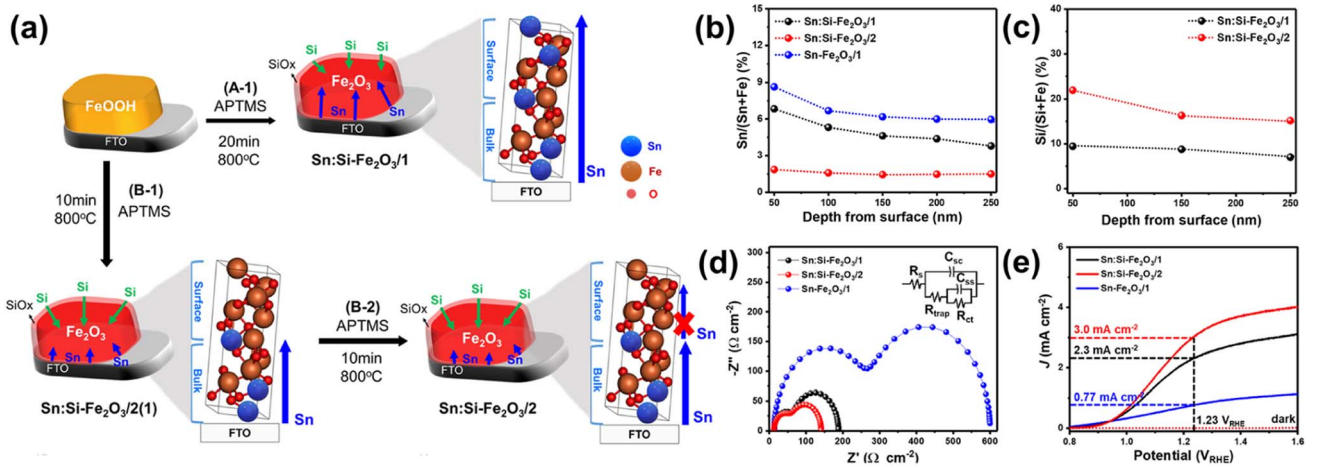

Fig. 12 (a) Fabrication procedures of Sn:Si-Fe_2O_3/1 and Sn:Si-Fe_2O_3/2. (b) XPS depth profiles of Si and (c) Sn according to the depth from the surface of Sn:Si-Fe_2O_3/1–2. (d) EIS measurements at 1.23 V_{RHE}, and (e) *J*–*V* curves of Sn:Si-Fe_2O_3/1–2, and Sn-Fe_2O_3/1. Reproduced from ref. 65 with permission from American Chemical Society, Copyright 2021.

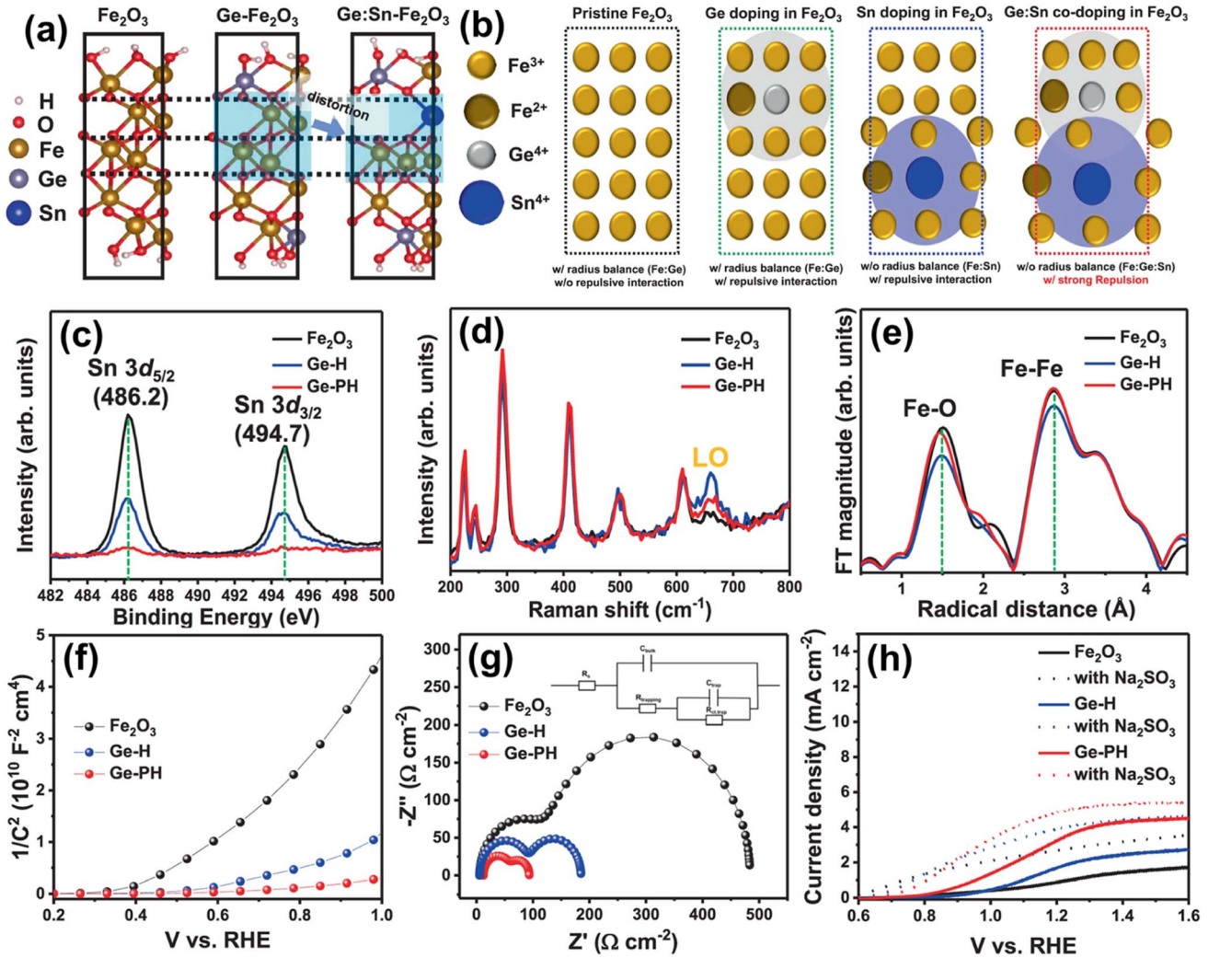

Fig. 13 (a) DFT calculations of atomic arrangements of Fe_2O_3 with different dopant environments. (b) Atomic structure of Ge-doped Fe_2O_3 Sn-doped Fe_2O_3 and Ge:Sn co-doped Fe_2O_3. (c) XPS spectra of Sn. (d) Raman spectra. (e) Fourier transform of the EXAFS data at the Fe k-edge of the hematite nanostructures. (f) Mott–Schottky plots and (g) EIS measurements (with the circuit model). (h) *J*–*V* curves of Fe_2O_3, Ge-H, and Ge-PH under illumination in 1 M NaOH (solid line) and a solution mixture of 1 M NaOH and 0.5 M Na_2SO_3 (dashed lines). Reproduced from ref. 67 with permission from Springer Nature, Copyright 2021.

co-doping system further, promising solutions have been proposed, focusing on the control of Sn diffusion from the substrate. Specifically, our investigation delved into the interactions between different dopants and Sn in the co-doped hematite photoanodes, which utilize the common FTO substrate.

Up to now, the highest efficiency of the hematite-based photoanode has been about 7 mA cm^{-2} at 1.23 V_{RHE}, and the efficiency has been increasing at a fairly rapid rate.[76] However, in order to reach the theoretical efficiency of about 12 mA cm^{-2} at 1.23 V_{RHE}, in addition to the synergistic effect between the substrate and other multiple dopants covered in this review, further study on the various components and different aspects of doping such as single atomic-level engineering is required.[50,51]

4. Summary and outlook

This review focused on the effects of Sn diffusion from the FTO substrate and the strategies used to control Sn diffusion *via* multiple dopants. Prior research has shown that moderate levels of Sn doping can enhance the PEC efficiency of a hematite photoanode. However, when combined with multiple dopants in the hematite lattice, Sn doping might exhibit detrimental effects. Consequently, to establish a more systematic approach to the hematite co-doping system, it is essential to design a more sophisticated doping system by considering the positive or negative interaction between the dopant and unintentional dopant Sn necessarily originating from the experimental process.

Efforts to improve solar energy conversion efficiency have focused on the individual efficiencies of sequential photocatalysis courses, including light harvesting, charge separation, and charge transport for solar fuel generation. Numerous studies have independently addressed these limitations, leading to significant improvements.

Nevertheless, to further boost efficiency and establish a cohesive system, it is imperative to concurrently consider the

synergistic impacts of the various dopants and PEC components discussed in this review.

Conflicts of interest

There are no conflicts of interest to declare.

Acknowledgements

This work was supported by the National Research Foundation of Korea (NRF) grant funded by the Korea government (MSIT) (No. NRF-2019M1A2A2065612, NRF-2020R1A2C2014050, and NRF-2020R1A5A1019631).

References

1 A. Fujishima and K. Honda, *Nature*, 1972, **238**, 37–38.
2 W. Yang, R. R. Prabhakar, J. Tan, S. D. Tilley and J. Moon, *Chem. Soc. Rev.*, 2019, **48**, 4979–5015.
3 R.-T. Gao, N. T. Nguyen, T. Nakajima, J. He, X. Liu, X. Zhang, L. Wang and L. Wu, *Sci. Adv.*, 2023, **9**, eade4589.
4 C. Avcıoğlu, S. Avcıoğlu, M. F. Bekheet and A. Gurlo, *Mater. Today Energy*, 2022, **24**, 100936.
5 Y. Yang, S. Niu, D. Han, T. Liu, G. Wang and Y. Li, *Adv. Energy Mater.*, 2017, **7**, 1700555.
6 T. Hisatomi, J. Kubota and K. Domen, *Chem. Soc. Rev.*, 2014, **43**, 7520–7535.
7 K. Kim, P. Thiyagarajan, H.-J. Ahn, S.-I. Kim and J.-H. Jang, *Nanoscale*, 2013, **5**, 6254–6260.
8 H. G. Cha and K.-S. Choi, *Nat. Chem.*, 2015, **7**, 328–333.
9 Y. Kuang, T. Yamada and K. Domen, *Joule*, 2017, **1**, 290–305.
10 J. Seo, H. Nishiyama, T. Yamada and K. Domen, *Angew. Chem., Int. Ed.*, 2018, **57**, 8396–8415.
11 J. H. Kim and J. S. Lee, *Adv. Mater.*, 2019, **31**, 1806938.
12 X. T. Xu, L. Pan, X. Zhang, L. Wang and J. J. Zou, *Adv. Sci.*, 2019, **6**, 1801505.
13 A. G. Tamirat, J. Rick, A. A. Dubale, W.-N. Su and B.-J. Hwang, *Nanoscale Horiz.*, 2016, **1**, 243–267.
14 D. K. Lee, D. Lee, M. A. Lumley and K.-S. Choi, *Chem. Soc. Rev.*, 2019, **48**, 2126–2157.
15 K.-Y. Yoon, H.-J. Ahn, M.-J. Kwak, S.-I. Kim, J. Park and J.-H. Jang, *J. Mater. Chem. A*, 2016, **4**, 18730–18736.
16 C. Jiang, S. J. Moniz, A. Wang, T. Zhang and J. Tang, *Chem. Soc. Rev.*, 2017, **46**, 4645–4660.
17 K. Arifin, R. M. Yunus, L. J. Minggu and M. B. Kassim, *Int. J. Hydrogen Energy*, 2021, **46**, 4998–5024.
18 H.-J. Ahn, M.-J. Kwak, J.-S. Lee, K.-Y. Yoon and J.-H. Jang, *J. Mater. Chem. A*, 2014, **2**, 19999–20003.
19 X. Liu, F. Wang and Q. Wang, *Phys. Chem. Chem. Phys.*, 2012, **14**, 7894–7911.
20 P. Sharma, J. W. Jang and J. S. Lee, *ChemCatChem*, 2019, **11**, 157–179.
21 P. Thiyagarajan, H. J. Ahn, J. S. Lee, J. C. Yoon and J. H. Jang, *Small*, 2013, **9**, 2341–2347.
22 R.-T. Gao, D. He, L. Wu, K. Hu, X. Liu, Y. Su and L. Wang, *Angew. Chem., Int. Ed.*, 2020, **59**, 6213–6218.
23 R. T. Gao and L. Wang, *Angew. Chem., Int. Ed.*, 2020, **59**, 23094–23099.
24 H. Shi, H. Guo, S. Wang, G. Zhang, Y. Hu, W. Jiang and G. Liu, *Energy Fuels*, 2022, **36**, 11404–11427.
25 D. K. Lee and K.-S. Choi, *Nat. Energy*, 2018, **3**, 53–60.
26 G. Wang, Y. Yang, Y. Ling, H. Wang, X. Lu, Y.-C. Pu, J. Z. Zhang, Y. Tong and Y. Li, *J. Mater. Chem. A*, 2016, **4**, 2849–2855.
27 P. Liao, M. C. Toroker and E. A. Carter, *Nano Lett.*, 2011, **11**, 1775–1781.
28 Z. Zhou, P. Huo, L. Guo and O. V. Prezhdo, *J. Phys. Chem. C*, 2015, **119**, 26303–26310.
29 A. Alarawi, V. Ramalingam and J.-H. He, *Mater. Today Energy*, 2019, **11**, 1–23.
30 K. Sivula, F. Le Formal and M. Grätzel, *ChemSusChem*, 2011, **4**, 432–449.
31 T. W. Hamann, *Dalton Trans.*, 2012, **41**, 7830–7834.
32 H. Chai, S. Wang, X. Wang, J. Ma and J. Jin, *ACS Catal.*, 2022, **12**, 3700–3709.
33 S. Shen, S. A. Lindley, X. Chen and J. Z. Zhang, *Energy Environ. Sci.*, 2016, **9**, 2744–2775.
34 C. Li, Z. Luo, T. Wang and J. Gong, *Adv. Mater.*, 2018, **30**, 1707502.
35 B. Iandolo, B. Wickman, I. Zorić and A. Hellman, *J. Mater. Chem. A*, 2015, **3**, 16896–16912.
36 J. Park, K.-Y. Yoon, M.-J. Kwak, J. Kang, S. Kim, S. Chaule, S.-J. Ha and J.-H. Jang, *ACS Appl. Mater. Interfaces*, 2023, **15**, 9341–9349.
37 Y. Lin, G. Yuan, S. Sheehan, S. Zhou and D. Wang, *Energy Environ. Sci.*, 2011, **4**, 4862–4869.
38 K. Kim, I.-H. Kim, K.-Y. Yoon, J. Lee and J.-H. Jang, *J. Mater. Chem. A*, 2015, **3**, 7706–7709.
39 T. Hisatomi, H. Dotan, M. Stefik, K. Sivula, A. Rothschild, M. Grätzel and N. Mathews, *Adv. Mater.*, 2012, **24**, 2699–2702.
40 L. Steier, I. Herraiz-Cardona, S. Gimenez, F. Fabregat-Santiago, J. Bisquert, S. D. Tilley and M. Grätzel, *Adv. Funct. Mater.*, 2014, **24**, 7681–7688.
41 H.-J. Ahn, K.-Y. Yoon, M. Sung, H. Yoo, H. Ahn, B. H. Lee, J. Lee and J.-H. Jang, *ACS Energy Lett.*, 2023, **8**, 2595–2602.
42 C. H. Bak, K. Kim, K. Jung, J.-B. Kim and J.-H. Jang, *J. Mater. Chem. A*, 2014, **2**, 17249–17252.
43 H. J. Ahn, M. J. Kim, K. Kim, M. J. Kwak and J. H. Jang, *Small*, 2014, **10**, 2325–2330.
44 H.-J. Ahn, K.-Y. Yoon, M.-J. Kwak, J. Park and J.-H. Jang, *ACS Catal.*, 2018, **8**, 11932–11939.
45 S. Wang, C. Meng, Y. Bai, Y. Wang, P. Liu, L. Pan, L. Zhang, Z. Yin and N. Tang, *ACS Appl. Nano Mater.*, 2022, **5**, 6781–6791.
46 F. Li, J. Li, F. Li, L. Gao, X. Long, Y. Hu, C. Wang, S. Wei, J. Jin and J. Ma, *J. Mater. Chem. A*, 2018, **6**, 13412–13418.
47 Y. Lin, Y. Xu, M. T. Mayer, Z. I. Simpson, G. McMahon, S. Zhou and D. Wang, *J. Am. Chem. Soc.*, 2012, **134**, 5508–5511.
48 A. Kleiman-Shwarsctein, M. N. Huda, A. Walsh, Y. Yan, G. D. Stucky, Y.-S. Hu, M. M. Al-Jassim and E. W. McFarland, *Chem. Mater.*, 2010, **22**, 510–517.

49 R. Rivera, H. P. Pinto, A. Stashans and L. Piedra, *Phys. Scr.*, 2011, **85**, 015602.
50 R.-T. Gao, L. Liu, Y. Li, Y. Yang, J. He, X. Liu, X. Zhang, L. Wang and L. Wu, *Proc. Natl. Acad. Sci. U. S. A.*, 2023, **120**, e2300493120.
51 R.-T. Gao, J. Zhang, T. Nakajima, J. He, X. Liu, X. Zhang, L. Wang and L. Wu, *Nat. Commun.*, 2023, **14**, 2640.
52 H.-J. Ahn, K.-Y. Yoon, M.-J. Kwak and J.-H. Jang, *Angew. Chem., Int. Ed.*, 2016, **55**, 9922–9926.
53 Y. F. Xu, X. D. Wang, H. Y. Chen, D. B. Kuang and C. Y. Su, *Adv. Funct. Mater.*, 2016, **26**, 4414–4421.
54 Y. Zhang, S. Jiang, W. Song, P. Zhou, H. Ji, W. Ma, W. Hao, C. Chen and J. Zhao, *Energy Environ. Sci.*, 2015, **8**, 1231–1236.
55 Z. Luo, C. Li, S. Liu, T. Wang and J. Gong, *Chem. Sci.*, 2017, **8**, 91–100.
56 J. Kang, K.-Y. Yoon, J.-E. Lee, J. Park, S. Chaule and J.-H. Jang, *Nano Energy*, 2023, **107**, 108090.
57 A. Kay, I. Cesar and M. Grätzel, *J. Am. Chem. Soc.*, 2006, **128**, 15714–15721.
58 J. Park, K.-Y. Yoon, T. Kim, H. Jang, M.-J. Kwak, J. Y. Kim and J.-H. Jang, *Nano Energy*, 2020, **76**, 105089.
59 K.-Y. Yoon, J. Park, H. Lee, J. H. Seo, M.-J. Kwak, J. H. Lee and J.-H. Jang, *ACS Catal.*, 2022, **12**, 5112–5122.
60 K. Sivula, R. Zboril, F. Le Formal, R. Robert, A. Weidenkaff, J. Tucek, J. Frydrych and M. Gratzel, *J. Am. Chem. Soc.*, 2010, **132**, 7436–7444.
61 Y. Ling, G. Wang, D. A. Wheeler, J. Z. Zhang and Y. Li, *Nano Lett.*, 2011, **11**, 2119–2125.
62 A. Annamalai, A. Subramanian, U. Kang, H. Park, S. H. Choi and J. S. Jang, *J. Phys. Chem. C*, 2015, **119**, 3810–3817.
63 M. Li, Y. Yang, Y. Ling, W. Qiu, F. Wang, T. Liu, Y. Song, X. Liu, P. Fang and Y. Tong, *Nano Lett.*, 2017, **17**, 2490–2495.
64 A. Annamalai, H. H. Lee, S. H. Choi, S. Y. Lee, E. Gracia-Espino, A. Subramanian, J. Park, K.-j. Kong and J. S. Jang, *Sci. Rep.*, 2016, **6**, 23183.
65 J. Park, K.-Y. Yoon, M.-J. Kwak, J.-E. Lee, J. Kang and J.-H. Jang, *ACS Appl. Mater. Interfaces*, 2021, **13**, 54906–54915.
66 J. Liu, Y. Cai, Z. Tian, G. Ruan, Y. Ye, C. Liang and G. Shao, *Nano Energy*, 2014, **9**, 282–290.
67 K.-Y. Yoon, J. Park, M. Jung, S.-G. Ji, H. Lee, J. H. Seo, M.-J. Kwak, S. Il Seok, J. H. Lee and J.-H. Jang, *Nat. Commun.*, 2021, **12**, 4309.
68 Z. Fu, T. Jiang, L. Zhang, B. Liu, D. Wang, L. Wang and T. Xie, *J. Mater. Chem. A*, 2014, **2**, 13705–13712.
69 C. Li, A. Li, Z. Luo, J. Zhang, X. Chang, Z. Huang, T. Wang and J. Gong, *Angew. Chem.*, 2017, **129**, 4214–4219.
70 H. Zhang, D. Li, W. J. Byun, X. Wang, T. J. Shin, H. Y. Jeong, H. Han, C. Li and J. S. Lee, *Nat. Commun.*, 2020, **11**, 4622.
71 H. Zhang, W. Y. Noh, F. Li, J. H. Kim, H. Y. Jeong and J. S. Lee, *Adv. Funct. Mater.*, 2019, **29**, 1805737.
72 J. Y. Kim, G. Magesh, D. H. Youn, J.-W. Jang, J. Kubota, K. Domen and J. S. Lee, *Sci. Rep.*, 2013, **3**, 2681.
73 Y. Fu, C. L. Dong, W. Y. Lee, J. Chen, P. Guo, L. Zhao and S. Shen, *ChemNanoMat*, 2016, **2**, 704–711.
74 H. Zhang, J. H. Park, W. J. Byun, M. H. Song and J. S. Lee, *Chem. Sci.*, 2019, **10**, 10436–10444.
75 P. S. Shinde, A. Annamalai, J. H. Kim, S. H. Choi, J. S. Lee and J. S. Jang, *Sol. Energy Mater. Sol. Cells*, 2015, **141**, 71–79.
76 D. Hansora, D. Cherian, R. Mehrotra, J.-W. Jang and J. S. Lee, *Joule*, 2023, **7**, 884–919.